Cement and Concrete Research 115 (2019) 367–378

Contents lists available at ScienceDirect

Cement and Concrete Research

journal homepage: www.elsevier.com/locate/cemconres

The chemistry and structure of calcium (alumino) silicate hydrate: A study by XANES, ptychographic imaging, and wide- and small-angle scattering

Jiaqi Li[a,*], Guoqing Geng[a,b,*], Rupert Myers[a,c], Young-Sang Yu[d], David Shapiro[d], Carlo Carraro[e], Roya Maboudian[e], Paulo J.M. Monteiro[a,f]

[a] Department of Civil and Environmental Engineering, University of California, Berkeley, CA, United States
[b] Paul Scherrer Institute, Villigen, Switzerland
[c] School of Engineering, University of Edinburgh, Edinburgh, United Kingdom
[d] Advanced Light Source, Lawrence Berkeley National Laboratory, Berkeley, CA, United States
[e] Department of Chemical and Biomolecular Engineering, University of California, Berkeley, CA, United States
[f] Material Science Division, Lawrence Berkeley National Laboratory, Berkeley, CA, United States

ARTICLE INFO

Keywords:
Temperature
Calcium-silicate-hydrate
Third aluminate hydrate
Blended cement
C-A-S-H

ABSTRACT

Calcium (alumino)silicate hydrate (C-(A-)S-H) is the main binding phase in blended cement concrete. Understanding the chemistry and structure of C-(A-)S-H is essential to optimizing concrete properties such as compressive strength and durability; yet questions remain around the coordination environments of Ca and Al in its structure with various chemical compositions and equilibration temperatures. C-(A-)S-H with Ca/Si = 0.6–1.6, Al/Si = 0–0.1, and equilibrated at 7–80 °C is studied by nanoscale soft X-ray spectroscopy at the Ca $L_{2,3}$- and Si *K*-edges. Highly distorted CaO_7 complexes occur in the intralayer of C-(A-)S-H irrespective of Ca/Si, Al/Si, and temperature. Zeolitic Ca in the interlayer of C-(A-)S-H is highly distorted from an ideal octahedral coordination. Third aluminate hydrate is either not Ca-bearing or its Ca is structurally similar to C-(A-)S-H and does not resemble the Ca in AFm-phases. Increasing aluminosilicate chain polymerization in C-(A-)S-H shifts the Si *K*-edge to higher energies, implying Al uptake in the bridging and/or cross-linked sites, as well as a contraction of Si—O bond lengths. C-(A-)S-H exhibits a foil-like morphology, with individual foils comprised of nano-sized platelets with comparable thickness regardless of Ca/Si or Al/Si at 7–50 °C. Coarser C-(A-)S-H foils occur at 80 °C and higher Al/Si ratios relative to lower temperatures and Al content.

1. Introduction

Calcium (alumino)silicate hydrate (C-(A-)S-H)[1] is the main binding phase in blended cement concrete [1]. The Ca/Si ratio in calcium silicate hydrate (C-S-H) in hydrated Portland cement (PC) is ~1.7 [2]. The addition of supplementary cementitious materials (SCMs), e.g., fly ash and blast furnace slag, leads to the uptake of Al and a decrease in Ca/(Si + Al) ratio in this phase [3,4]. C-(A-)S-H equilibrated at room temperature is structurally analogous to defective tobermorite, which contains calcium oxide polyhedra sheets flanked with "dreierketten" – tetrahedral (alumino)silicate chains – on one side and counter-ions (e.g., Ca and alkalis) and water in an interlayer on the other [5–9]. At Ca/Si < 0.6–0.8, long silicate tetrahedral chains occur, which predominantly consist of repeating units of one bridging site (Q^2_B)[2] connected to two paired silicate tetrahedral sites (Q^2_P) on either side. At higher Ca/Si ratios > ~1.0 these chains are significantly shorter albeit structurally similar, and have varying degrees of vacant tetrahedra in bridging sites [10].

Aluminum incorporated into these chains occurs in tetrahedral AlO_4 sites. Five-fold coordinated aluminum (Al^V) and six-fold coordinated Al ($Al^{VI\text{-}a}$) have also been identified to occur in C-(A-)S-H [11–13]. Increased availability of Al favors the precipitation of katoite (C_3AH_6) and strätlingite (C_2ASH_8) as secondary products, which become increasingly stable relative to Al uptake in C-(A-)S-H at higher Al concentrations. These conditions also promote the precipitation of octahedral Al ($Al^{VI\text{-}b}$) in a (calcium) aluminate hydrate phase (also termed as the third aluminum hydrate, TAH) [14–16]. The nature and location of this phase remain unclear. Substitution of Si for Al in C-A-S-H occurs

* Corresponding authors at: 115 Davis Hall, University of California at Berkeley, Berkeley, CA 94720, United States.
E-mail addresses: Jiaqi.li@berkeley.edu (J. Li), guoqing_geng@berkeley.edu (G. Geng).

[1] Cement chemistry shorthand notation is used throughout the text: A, Al_2O_3; C, CaO; H, H_2O; S, SiO_2; and $\bar{S}$, SO_3.

[2] Here, $Q^n(mAl)$ designates a SiO_4 tetrahedron that is connected to *m* AlO_4 tetrahedra and *n* aluminosilicate tetrahedra.

https://doi.org/10.1016/j.cemconres.2018.09.008
Received 23 February 2018; Received in revised form 8 June 2018; Accepted 21 September 2018
Available online 26 September 2018
0008-8846/ © 2018 Elsevier Ltd. All rights reserved.

preferably in bridging sites. Si for Al substitution also occurs in cross-linked bridging sites (Q^3) at 80 °C, and in alkali-activated fly ash and slag at room temperature [12,17–19]. Note that, the solubility and coordination of Al are pH dependent; the pH of pore solution of hardened concrete typically is 13–14 [20].

One major continuing debate in existing C-S-H models [21–25] is the coordination of Ca in C-S-H. An extended X-ray absorption fine structure (EXAFS) study showed that Ca is octahedrally coordinated in C-S-H at Ca/Si ratios of 0.7–1.4, and in 11 Å and 14 Å tobermorite [26], the results do not agree with XRD data of tobermorite [27]. XRD results from Merlino and Bonacorrsi [5–9,27–30] clearly showed that the coordination number of Ca of 11 Å- and 14 Å-tobermorite is seven and/or six. Kirkpatrick et al. [31] reported distinct values for the average coordination numbers of Ca: 5.5–6.2 for C-S-H(I), 6.1 for 11 Å tobermorite, and 6.9 for 14 Å tobermorite. A pair distribution function (PDF) study showed that the average coordination number of Ca in synthetic C-S-H systematically decreases from 7.1 to 6.0 as Ca/Si ratio increases [32]. ^{43}Ca nuclear magnetic resonance (NMR) analysis showed that Ca environments in C-S-H are similar to 11 Å tobermorite at Ca/Si ≤ 1.5 [33]. A C-S-H model with octahedral Ca—O sheet for accommodating Al was proposed [22]. Coordination numbers of Ca in thirty five crystalline C-S-H and related minerals were mainly found to be six or seven, with a small number of eight-fold Ca atoms [34]. There is consensus that the coordination number of Ca in C-S-H is between 6 and 7 although it remains unclear how the coordination symmetry of CaO_x complexes varies with Al incorporation and equilibration temperature.

Transmission electron microscopy (TEM) studies have shown that 'outer product' C-S-H is fibrillar in hydrated PC pastes and foil like in hydrated PC-slag blends [2,23,35–38]. The morphology of C-S-H with various Ca/Si and equilibration conditions varies from foil to fiber-like [39]. However, the effects of chemical compositions and equilibration temperatures on the morphology of synthetic C-A-S-H have not been extensively studied. The sample preparation and high accelerating voltage of TEM can damage C-(A-)S-H samples [40], limiting its use in characterizing these materials. Ptychographic imaging using synchrotron-based X-ray radiation has only relatively recently been applied to characterize the morphology of cement-based materials [41,42]. It yields image resolutions of 10 nm or better while, for many materials, results in less damage compared to TEM. Coupled with scanning transmission X-ray microscopy (STXM), it enables comprehensive nanometer-resolved spectroscopic investigation of cementitious materials. Preliminary STXM studies have shown a strong correlation between the degree of polymerization of silicate chains and features in X-ray Absorption Near Edge Structure (XANES) spectra at the Si *K*-edge [43–45]. However, more experimental work is needed to obtain Si *K*-edge XANES spectra of C-(A-)S-H covering the full range of compositions and temperatures applicable to hydrated PC/SCM blends.

This paper aims to use STXM, coupled with ptychographic imaging, to provide new insights into the effects of bulk Ca/Si molar ratios (0.6–1.6), bulk Al/Si molar ratios (0–0.1), and equilibration temperatures at 7, 20, 50, and 80 °C on the atomic environment of Ca, Si, and Al in C-(A-)S-H. The experimental setup here provides state-of-the-art spatially resolved (~10 nm) chemical information of C-(A-)S-H and intermixed secondary phases. Results are used to unveil the chemistry and nano-morphology of these phases, and also correlate the degree of polymerization of its (alumino)silicate chains with features in Ca $L_{2,3}$- and Si *K*-edges XANES spectra.

2. Materials and methods

2.1. Materials

C-(A-)S-H samples were synthesized at initial bulk Ca/Si molar ratios (Ca/Si*) of 0.6, 0.8, 1.0, 1.2, 1.4 and 1.6, bulk Al/Si molar ratios (Al/Si*) of 0 and 0.05, and cured at 20 °C for 182 days by mixing stoichiometric amounts of SiO_2 (Aerosil 200, Evonik), CaO (prepared by calcining $CaCO_3$ (Merck Millipore) at 1000 °C for 12 h) and $CaO{\cdot}Al_2O_3$ at a water/solid ratio of 45 in a N_2-filled glove box. Additional samples with Ca/Si* = 1 and Al/Si* of 0, 0.05 and 0.1 were water bathed at 7 °C for one year, and at 50 and 80 °C for 56 days. The solid C-(A-)S-H samples were vacuum filtered by using 0.45 μm nylon filter papers, freeze-dried for 7 days, and then stored in N_2-filled desiccators in the presence of saturated $CaCl_2$ solutions and NaOH pellets. Full details of these procedures are provided in [46].

2.2. Methods

2.2.1. XANES/STXM

XANES spectra of the C-(A-)S-H samples were obtained using STXM at bending magnet beamlines 5.3.2.1 and 5.3.2.2 at the Advanced Light Source (ALS) of the Lawrence Berkeley National Laboratory (LBNL) [47]. The STXM beamlines use synchrotron X-ray radiation as the incident beam. The monochromatic X-ray is focused using a zone plate onto the samples that are mounted on a multi-motor stage inside a vacuum chamber (base pressure of 200 mTorr). The downstream phosphor-photomultiplier tube (PMT) records the transmitted X-ray intensity as a function of the tuned beam energy. Depending on the scanning mode, e.g., line-scan and area-scan, the absorption data of the scanned locations can be generated and assessed using suitable software, e.g., A*xis2000* [45]. In this study, XANES spectra at Si *K*-edge (1830–1880 eV) were measured in line scan mode with an energy resolution of 0.3 eV and a dwell time of 50 ms; spectra at Ca $L_{2,3}$-edge (345–356 eV) were obtained in line scan mode at an energy resolution of 0.1 eV with a dwell time of 30 ms. A comprehensive description of the STXM beamlines is given in [48].

2.2.2. X-ray ptychography

X-ray ptychographic images were obtained at 800 eV at beamline 5.3.2.1 at ALS, using the STXM setup described above except a fast CCD detector was used. Details of the imaging method are reported in [39]. In brief, it uses scanning steps smaller than the beam spot, i.e., the adjacent illuminated spots are greatly overlapped. The cluster-based codes reconstruct both the real and imaginary parts of the transmitted X-ray beam in each scanning step, which then yield high-resolution images using either magnitude or phase information as the contrast. The pixel size in this study is 5 nm, although the actual spatial resolution (smallest resolvable features as determined by the amount of scattering from the sample) is estimated to be ~10 nm. To avoid X-ray beam absorption saturation, the C-(A-)S-H samples were gently dispersed in polystyrene weigh boats (Fisherbrand) using isopropanol (> 99.5% purity, Fisher Chemical) with liquid-to-solid mass ratio of 10 and dropped in between two Si_3N_4 windows (100-nm-thick, Norcada). To quantify the morphological information obtained using ptychography, we integrated small angle scattering (SAS) by calculating small angle scattering patterns from the ptychographic magnitude images. A lamellar Guinier–Porod model was used to fit the patterns, which enable the sizes of the C-(A-)S-H particles to be estimated. More details are shown in Supplementary information.

3. Results and discussion

3.1. Ca coordination

3.1.1. Ca/Si* = 0.6–1.6, Al/Si* = 0, and equilibrium at 20 °C

The Ca $L_{2,3}$-edge spectra of the C-(A-)S-H samples (Figs. 1 and 2) resemble $L_{2,3}$-edge spectra of d^0 compounds, e.g., Ca^{2+} and K^+. They correspond to the excitation of Ca atoms from $2p^63d^0$ to $2p^53d^1$. Due to the loss of degeneracy of 2*p* orbitals by spin-orbit coupling, two major peaks are observed, L_3 ($2p_{3/2}$, a_2 peak) and L_2 ($2p_{1/2}$, b_2 peak) [49]. Minor peaks (a_1 and b_1) exist to the left of each major peak, which originate from crystal field splitting. These peaks are clearly observed

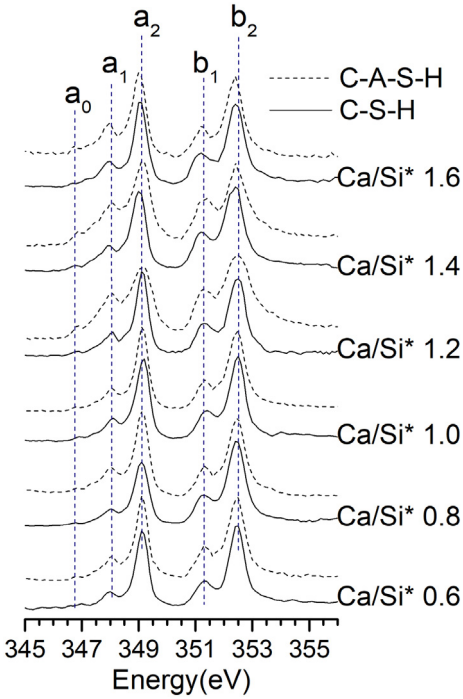

Fig. 1. Ca $L_{2,3}$-edge XANES spectra of C-S-H (solid lines) and C-A-S-H with Al/Si* = 0.05 (dashed lines) after 182 days of hydration at 20 °C. Ca/Si* = bulk Ca/Si.

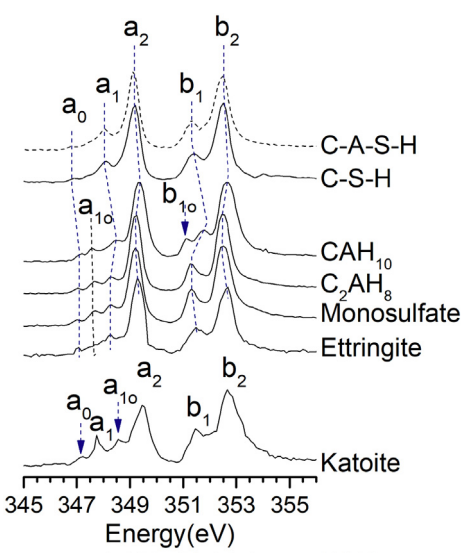

Fig. 2. Ca $L_{2,3}$-edge XANES spectra of C-S-H (solid lines) and C-A-S-H (dashed lines, Al/Si* = 0.05) after 182 days of hydration at 20 °C. Spectra of CAH_{10}, C_2AH_8, monosulfoaluminate (monosulfate, $C_4A\bar{S}H_{12}$), ettringite ($C_6A\bar{S}_3H_{32}$) and katoite (C_3AH_6) are taken from [41]. Ca/Si* = bulk Ca/Si.

when the coordination configuration is of a certain symmetry, e.g., octahedral or cubic. The energy separations (splitting energies, $\Delta L_3 = a_2 - a_1$ and $\Delta L_2 = b_2 - b_1$) in two doublets between the adjacent major and minor peaks relate to the strength of the crystal field effects, which depend on the ligand type and distortion of the symmetry [50]. A small leading peak a_0 originates from the mixing of states due to multipole interactions of core holes with valence electrons, combined with 3*d* spin-orbit splitting effects [51].

The spectra indicate that Ca possesses an octahedral-like coordination symmetry in all samples. However, this symmetry is clearly distorted since the a_1 and b_1 peaks are not as sharp and intense as those in $Ca(OH)_2$ spectra, where Ca is in an ideal octahedral symmetry. The pre-edge peak a_0 is less resolvable in C-S-H samples than in C-A-S-H samples due to the poorer crystallinity of C-S-H. The Ca in the studied samples are not cubic-coordinated, else an extra minor peak would be visible between a_1 and a_2 peaks (katoite-like) [52].

For samples with Ca/Si* in the range of 0.6–1.4, the splitting energies of C-S-H are consistently near 1.1 eV (see Table 1), suggesting that most Ca in C-S-H are in similar coordination environments. The low peak intensity ratios between minor and major peaks suggest that there is no tendency to form a well-crystallized phase as Ca/Si increases [43,49,53,54]. In addition, a strong splitting is not observed in C-S-H with Ca/Si* = 1.6 when the scanned step is refined to ~20 nm. The absence of strong splitting suggests that the small amount of portlandite in bulk X-ray diffraction (XRD) results [46] forms distinct (micro) crystallites, and does not regularly intermix with C-(A-)S-H at the length scale of 20 nm. This interpretation is consistent with the previous assignment of a Ca/Si ratio of 1.38 to this C-S-H phase in this sample, with the remaining Ca in this sample assigned to a distinct portlandite phase (Ca/Si* = 1.6) [55]. Our results are also consistent with the interpretation that the Ca/Si* = 1.6 sample is not fully equilibrated [56], because at this composition and at equilibrium phase pure C-S-H is stable [57]. Therefore, the Ca $L_{2,3}$-edge spectra are fully explained by a defective tobermorite based model [58], i.e., the low splitting energy at Ca $L_{2,3}$-edge originates mainly from the seven-fold coordinated Ca—O sheet in the intralayer of C-S-H, and has minor contribution from the octahedral coordinated zeolitic Ca that is charge-balanced in the interlayer. As Ca/Si increases, there is no increasing trend of the peak intensity ratios between minor and major peaks, indicating that the increasing amount of the interlayer Ca is six-fold coordinated in a highly distorted octahedral symmetry, which is consistent with our interpretation. The interlayer $[Ca(H_2O)_6]^{2+}$ at Ca/Si ≤ 1.5 and $[Ca(OH)(H_2O)_5]^{+}$ at Ca/Si* = 1.6 suggested by Gartner et al. [59] are both with highly distorted octahedral symmetry, which is consistent with our interpretation. Furthermore, the PDF work reported that the interlayer Ca in C-S-H with high Ca/Si ratios (> 1.2) is more likely octahedrally coordinated [32].

The major peak positions (a_2 and b_2) in the spectra for C-S-H with Ca/Si* = 0.6–1.2 are generally equivalent, suggesting a comparable oxidation degree of Ca and a similar average coordination number of Ca—O in C-S-H at low Ca/Si*. For Ca/Si* of 1.4 and 1.6, the major peak positions are 0.05–0.1 eV lower than those at Ca/Si* ≤ 1.2, suggesting that more six-fold coordinated zeolitic Ca species are charge-balanced in the interlayer or on the surface of C-S-H in this higher Ca/Si* range. The occurrence of seven- and/or six-fold Ca sites in C-S-H(I) is in good agreement with 11 Å- and 14 Å-tobermorite, the Ca—O coordination numbers of which are mostly six or seven [5,27,34]. The reported X-ray photoelectron spectroscopy experiments exhibit similar results, namely, a Ca $2p_{3/2}$ binding energy of C-S-H [60] that is independent of the Ca/Si ratio.

3.1.2. Ca/Si = 0.6–1.6, Al/Si* = 0.05, and equilibrium at 20 °C*

Comparable peak positions are identified in the Ca $L_{2,3}$-edge spectra for the C-A-S-H and C-S-H samples equilibrated at 20 °C, indicating that minor Al uptake (Al/Si* = 0.05) does not greatly alter the coordination of Ca—O complexes in their structures, regardless of Ca/Si ratio. At Ca/Si* = 1.4 and 1.6, the major peaks in the C-A-S-H spectra are positioned at slightly higher energies than in the C-S-H spectra. We assign this effect to the higher ordering of CaO_7 due to Al incorporation by elongating silicate chains and CaO_7 sheets. Compared to the peak intensity ratios (a_1/a_2 and b_1/b_2) of C-S-H, the C-A-S-H spectra exhibit marginally higher values, which suggests an increase in the long-range order of CaO_7 sheet due to Al incorporation. However, Al incorporation does not increase the coordination symmetry of Ca—O complexes in C-(A-)S-H structure since its splitting energies are still comparable to C-S-H.

Fig. 2 shows the Ca $L_{2,3}$-edge XANES spectra of Ca—O complexes in C-(A-)S-H and in other cement-related phases [41]. Katoite was

Table 1
Features in the Ca $L_{2,3}$-edge XANES spectra of C-(A-)S-H samples. The estimated absolute errors are ± 0.01 eV in energy positions and ± 0.0002 units in intensity ratios.

Al/Si*	Ca/Si*	Energy (eV)								
		a_0	a_1	a_2	a_1/a_2	ΔL_3	b_1	b_2	b_1/b_2	ΔL_2
Equilibrium at 20 °C										
0	0.6	347	348.0	349.1	0.0648	1.1	351.4	352.5	0.0944	1.1
	0.8	346.8	348.0	349.1	0.0618	1.1	351.35	352.45	0.0647	1.1
	1.0	348.8	348.0	349.1	0.0495	1.1	351.4	352.5	0.0756	1.1
	1.2	346.8	348.05	349.1	0.089	1.05	351.4	352.5	0.089	1.1
	1.4	346.8	347.95	349.0	0.0695	1.05	351.3	352.4	0.0935	1.1
	1.6	346.8	347.95	349.05	0.0842	1.1	351.25	352.4	0.1015	1.15
0.05	0.6	346.7	348.0	349.1	0.0992	1.1	351.4	352.5	0.1278	1.1
	0.8	346.8	348.0	349.1	0.0794	1.1	351.4	352.5	0.1382	1.1
	1.0	346.8	348.05	349.1	0.0798	1.05	351.45	352.5	0.1334	1.05
	1.2	346.8	348.0	349.1	0.144	1.1	351.4	352.5	0.1159	1.1
	1.4	346.8	348.0	349.1	0.0902	1.1	351.35	352.45	0.1501	1.1
	1.6	346.8	348.05	349.1	0.155	1.05	351.35	352.45	0.1482	1.1
Equilibrium at 7 °C										
0	1.0	347[a]	348.0[a]	349.1	–	1.1	351.4	352.5	0.017	1.1
0.05	1.0	347[a]	348.0[a]	349.1	0.0134	1.1	351.4	352.5	0.053	1.1
0.1	1.0	346.8[a]	348.0[a]	349.1	0.0433	1.1	351.4	352.5	0.0856	1.1
Equilibrium at 50 °C										
0	1.0	346.8	348.0	349.1	0.0814	1.1	351.35	352.5	0.0931	1.15
0.05	1.0	346.8	348.0	349.1	0.1188	1.1	351.4	352.5	0.1581	1.1
0.1	1.0	346.8	348.0	349.1	0.1303	1.1	351.4	352.5	0.171	1.1
Equilibrium at 80 °C										
0	1.0	346.8	348.0	349.1	0.0861	1.1	351.4	352.5	0.1688	1.1
0.05	1.0	346.8	348.0	349.1	0.1458	1.1	351.4	352.5	0.2241	1.1
0.1	1.0	346.8	348.0	349.1	0.1718	1.1	351.4	352.5	0.2557	1.1

[a] Weak peak, peak position is not clearly identified.

reported to form in the C-A-S-H samples that were analyzed here by L'Hôpital et al. using bulk XRD, thermogravimetric analysis, and ^{27}Al NMR measurements [56]. Yet the absence of the additional peak (a_{1o}) in this C-A-S-H phase on the sub-20 nm scale suggests that katoite does not intermix with C-A-S-H on this length scale. The major peak positions (a_2 and b_2) on C-A-S-H samples are identical to C_2AH_8 and monosulfate ($C_4A\bar{S}H_{12}$), which both have Ca coordination numbers of seven, and the major peak positions are ~0.2 eV lower than CAH_{10} and ettringite ($C_6A\bar{S}_3H_{32}$), which have Ca coordination numbers of eight. Therefore, we assign the coordination number of Ca in the CaO_x sheet of C-A-S-H to seven – the average coordination number of Ca in C-A-S-H is thus slightly smaller than seven due to the existence of minor quantities of octahedral Ca in the interlayer.

The absence of the leading a_{1o} and b_{1o} peaks in the Ca $L_{2,3}$-edge spectra, which are the characteristic peaks of AFm phases, AFm-like phases do not exist in C-A-S-H products. Furthermore, the Ca-O(H) complexes in C-A-S-H interlayer or on its surface are in octahedral-like coordination, although highly distorted. Renaudin et al. [61] proposed that calcium hydroxide, aluminum hydroxide, and an AFm-type calcium aluminate hydrate main layer may form in the interlayer of C-A-S-H. Andersen et al. [62] proposed that phases with octahedral Al may precipitate on C-A-S-H surfaces or as separate phases. The type of Ca found in AFm-type calcium aluminate hydrates is not identified in our Ca $L_{2,3}$-edge spectra on the sub-20 nm scale, indicating that TAH is not Ca-bearing or its Ca coordination environment is structurally analogous to Ca in C-(A-)S-H.

3.1.3. Ca/Si* = 1, Al/Si* = 0–0.1, and equilibrium at 7–80 °C

The peak positions in the Ca $L_{2,3}$-edge spectra for the C-(A-)S-H samples equilibrated at temperature ranging from 7 to 80 °C are found to be similar (Fig. 3 and Table 1). Therefore, the coordination numbers of Ca—O complexes in these samples are independent of equilibration temperature in this range. The coordination symmetry of Ca^{2+} in the interlayer of C-(A-)S-H is also clearly distorted regardless of the equilibration temperature. The slight increase in the relative intensity of

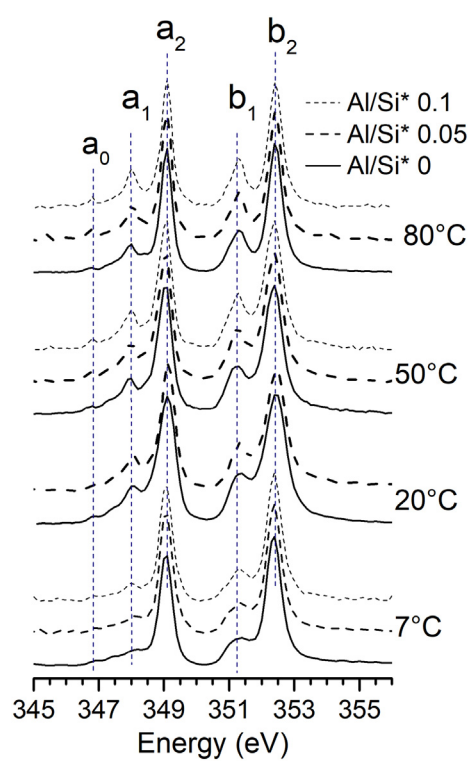

Fig. 3. Ca $L_{2,3}$-edge XANES spectra of C-S-H (solid lines, Al/Si* = 0, Ca/Si* = 1.0), C-A-S-H (long-dashed lines, Al/Si* = 0.05, Ca/Si* = 1.0), and C-A-S-H (short-dashed lines, Al/Si* = 0.1, Ca/Si* = 1.0) at different equilibration temperatures. Ca/Si* = bulk Ca/Si. Al/Si* = bulk Al/Si.

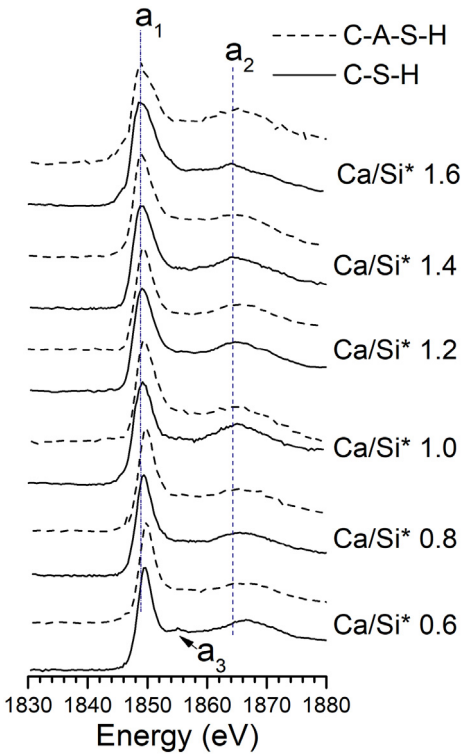

Fig. 4. Si *K*-edge XANES spectra of C-S-H (solid lines) and C-A-S-H with Al/Si* = 0.05 (dashed lines) after 182 days of equilibration at 20 °C. Ca/Si* = bulk Ca/Si. Al/Si* = bulk Al/Si.

Table 2
Peak positions and energy differences of Si *K*-edge XANES spectra of C-(A-)S-H equilibrated at 20 °C. The estimated absolute errors are ± 0.05 units in positions of peak a_1 and at Ca/Si = 0.6–1.2, ± 0.1 units in position of peak a_1 at Ca/Si = 1.4–1.6, and ± 0.15 units in position of peak a_2 and energy differences between peaks a_1 and a_2.

Ca/Si*	Peak a_1 (eV)	Peak a_2 (eV)	$\Delta a_2 - a_1$ (eV)
Al/Si* = 0			
0.6	1849.7	1866.6	16.9
0.8	1849.4	1865.6	16.2
1.0	1849.2	1865.1	15.9
1.2	1849.1	1864.8	15.7
1.4	1848.8	1864.6	15.4
1.6	1848.7	1864.0	15.3
Al/Si* = 0.05			
0.6	1849.8	1866.9	17.1
0.8	1849.5	1865.9	16.4
1.0	1849.3	1865.4	16.1
1.2	1849.2	1865.1	15.9
1.4	1849.0	1864.8	15.8
1.6	1849.0	1864.6	15.6

minor to major peaks (a_1/a_2 and b_1/b_2) with increasing equilibration temperature is observed in this temperature ranges and is attributed to increased long-range order of CaO_7 sheets in the C-(A-)S-H structure; the increment is more pronounced at 80 °C, indicating increased structural ordering in this sample. This result is consistent with [46], where the degree of stacking in the *c*-direction of C-(A-)S-H at 80 °C was observed to significantly increase. At each equilibration temperature, the relative intensity ratio of minor to major peaks slightly increases as Al incorporation increases, which suggests that CaO_7 sheets in C-A-S-H are more long range ordered than those in C-S-H. We attribute this effect to the more polymerized aluminosilicate chains in the C-A-S-H samples.

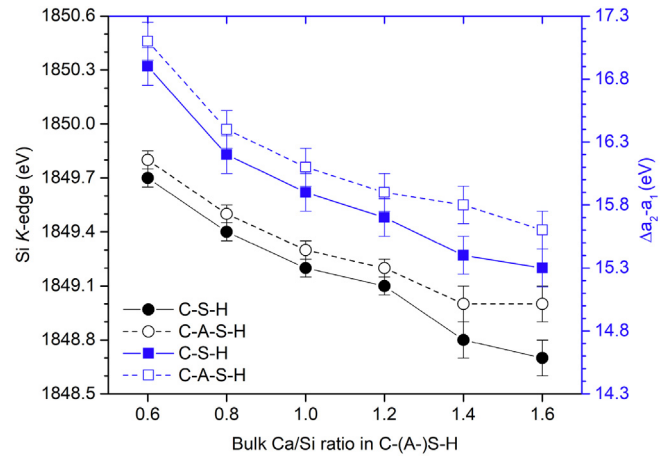

Fig. 5. Si *K*-edge energy and energy separation between major and minor peak ($\Delta a_2 - a_1$) as a function of Ca/Si* ratio of C-S-H (solid lines) and C-A-S-H with Al/Si* = 0.05 (dashed lines) after 182 days of equilibration at 20 °C.

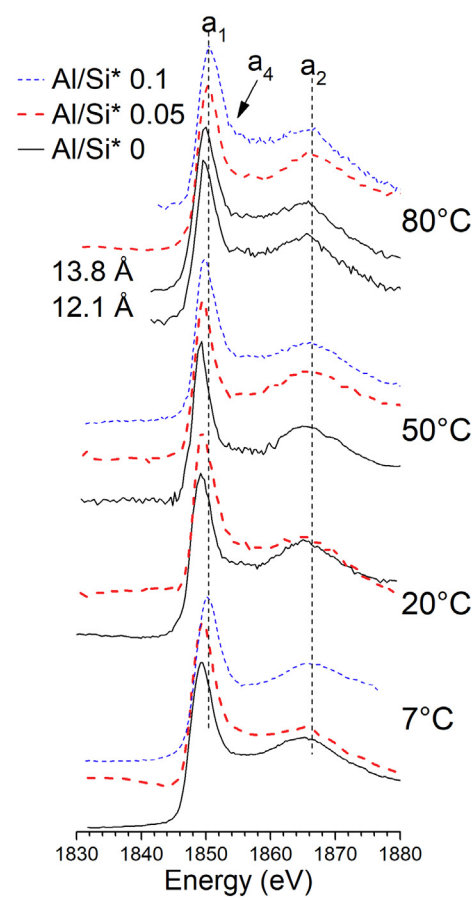

Fig. 6. Si *K*-edge XANES spectra of C-S-H (solid lines, Ca/Si* = 1.0), C-A-S-H (red long-dashed lines, Al/Si* = 0.05, Ca/Si* = 1.0), and C-A-S-H (blue short-dashed lines, Al/Si* = 0.1, Ca/Si* = 1.0) at different equilibration temperatures. The two C-S-H phases exist in the 80 °C sample, which are labeled with their average basal spacings. Ca/Si* = bulk Ca/Si. Al/Si* = bulk Al/Si. (For interpretation of the references to color in this figure legend, the reader is referred to the web version of this article.)

3.2. Chemical environment of Si

3.2.1. Ca/Si* = 0.6–1.6, Al/Si* = 0, and equilibrium at 20 °C

Fig. 4 shows the Si *K*-edge XANES spectra of C-(A-)S-H equilibrated at 20 °C. The major peak a_1 (Si *K*-edge peak) at 1848.7–1849.7 eV is

Table 3
Features of Si *K*-edge XANES spectra for C-(A-)S-H samples (Ca/Si* = 1) equilibrated at different temperatures. The estimated absolute errors are ± 0.05 units in positions of peak a_1 for C-(A-)S-H equilibrated at 7 °C–50 °C, ± 0.1 units in position of peak a_1 at for C-(A-)S-H equilibrated at 80 °C, and ± 0.15 units in position of peak a_2 and energy differences between peaks a_1 and a_2.

Al/Si*	Peak a_1 (eV)	Peak a_2 (eV)	$\Delta a_2 - a_1$ (eV)
Equilibrium at 7 °C			
0	1849.4	1865.3	15.9
0.05	1849.6	1865.6	16.0
0.1	1850.0	1866.2	16.2
Equilibrium at 20 °C			
0	1849.2	1865.1	15.9
0.05	1849.3	1865.4	16.1
Equilibrium at 50 °C			
0	1849.3	1865.1	15.8
0.05	1849.6	1865.7	16.1
0.1	1849.9	1866.1	16.2
Equilibrium at 80 °C			
0 (12.1 Å)	1849.6	1865.6	16.0
0 (13.8 Å)	1849.7	1865.8	16.1
0.05	1850.2	1866.5	16.3
0.1	1850.4	1866.9	16.5

The basal spacing shown in parentheses was measured by wide-angle X-ray scattering (WAXS, Appendix A in Supplementary information). Al/Si* = bulk Al/Si.

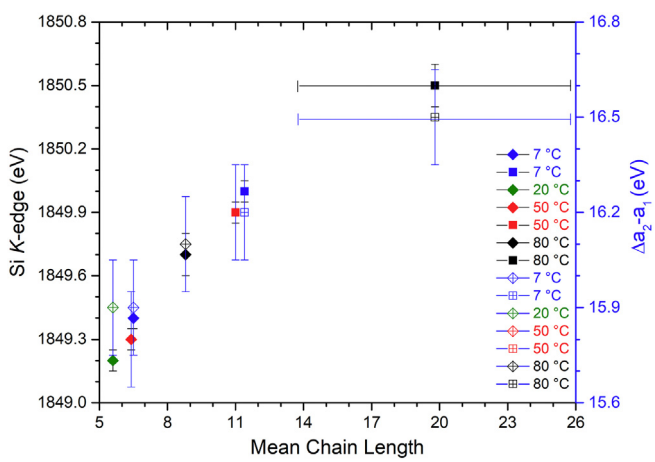

Fig. 7. Si *K*-edge energy and energy separation between major and minor peak ($\Delta a_2 - a_1$) as a function of the MCL of C-(A-)S-H equilibrated at 7–80 °C. The uncertainty of MCL (reproduced from [46]) is ± 1.25, except for the Al/Si* = 0.1 sample equilibrated at 80 °C, where the uncertainty of the MCL is represented by error bars. Al/Si* = 0.05 samples are marked as diamond and Al/Si* = 0.1 samples are marked as square. Al/Si* = bulk Al/Si.

assigned to the electronic transition from 1*s* to antibonding 3*p*-like state (t_2) in tetrahedrally symmetric Si (dipole allowed) [63]. The minor peaks a_2 (at ~1860–1867 eV) and a_3 (1853 eV) are attributable to multi-scattering effect from more distant atom shells through photoelectron interaction, particularly the second coordination shell, and its energy is governed by the interatomic distance [64]. The peak positions and energy separation between a_1 and a_2 peaks are listed in Table 2. A pre-edge peak presenting the transition of Si 1*s* electrons to the antibonding 3*s* orbital (dipole-forbidden) is only observed in the Ca/Si* = 1.6 C-S-H sample, suggesting the distortion of tetrahedral sites in the silicate chains.

As the Ca/Si ratio increases, the Si *K*-edges gradually shift to lower energy by 1 eV (Fig. 5). This effect is caused by the progressive increase in the electron shielding from more Ca and a reduction in the effective Si—O bond strength. The positive correlation between the location of the Si *K*-edge and the degree of silicate polymerization (i.e., mean chain length of silicate chains, MCL) in the C-S-H samples is consistent with previous work on silicate minerals [63,65].

The major and minor peak positions (a_1 and a_2) of C-S-H increase as the Ca/Si ratio decreases, suggesting a contraction of average Si—O bond lengths [66–69]. This trend is consistent with PDF analysis which showed slightly decreased average Si—O bond lengths as Ca/Si* decreases [32]. The inverse correlation between Si—O bond length and degree of silicate polymerization in the C-S-H samples with varying Ca/Si ratio is consistent with previous findings in many silicate minerals [69]. In general, the Si-O-Si bond angle is inversely correlated to Si—O bond length [70] (and thus directly related to the degree of silicate polymerization in C-S-H). Therefore, the shifted position of the Si *K*-edge to higher energies here implies that Si-O-Si bond angles in C-S-H increases as Ca/Si decreases. The Si *K*-edge peak a_1 sharpens with a decreased Ca/Si ratio, suggesting an increased long-range ordering of silicate tetrahedra [71]. This interpretation is consistent with previous studies on C-S-H materials, namely, as Ca/Si ratio decreases, (1) the ordering of Si—O—Si bond angles increases [72]; (2) the Si—O—Si bond angle broadens [73]; (3) the Si $2p_{3/2}$ and 2*s* binding energies increase [60,74]; and (4) the MCL of silicate chains in C-S-H increases [10]. Therefore, the energy difference between a_1 and a_2 peaks (Δ6) correlates to changing degrees of polymerization in these silicate chains (Fig. 5).

3.2.2. Ca/Si* = 0.6–1.6, Al/Si* = 0.05, and equilibrium at 20 °C

The energies of the Si *K*-edges in the spectra for the C-A-S-H samples increase by 0.1 to 0.3 eV with respect to C-S-H samples at each Ca/Si ratio increment (i.e., from Ca/Si* = 0.6 to 0.8, etc.) due to the increase in degree of polymerization of aluminosilicate chains (Figs. 4 and 5). The trend of increasing MCL with increasing Al in C-(A-)S-H is well known [13,56]. As the MCL in C-(A-)S-H increases, the electron shielding on Si from zeolitic Ca decreases, which corresponds to Si atoms effectively becoming more negatively charged. Increasing energies of the positions of Si *K*-edges in the spectra imply slight contractions of Si—O bonds in C-(A-)S-H. At Ca/Si* = 1.4 and 1.6, the increment of Si *K*-edge of C-A-S-H compared to C-S-H is 0.2 and 0.3 eV, respectively, which is slightly greater than that of C-A-S-H at lower Ca/Si ratio. This implies that aluminate tetrahedra link silicate dimers together and that Al prefers to occupy bridging sites, a significant proportion of which are vacant in C-S-H at Ca/Si ratios > 1.

Cross-linked Q^3 species are not clearly identified in C-A-S-H samples equilibrated at 20 °C, which is consistent with ^{29}Si NMR results of the same samples [56]. The Si *K*-edge peak, a_1 (1849 eV–1849.8 eV) of C-A-S-H is broadened compared to C-S-H and corresponds to Q^2(1Al) sites. As mentioned before, the energy of Si *K*-edge is dependent on the Si—O bong length and on the degree of silicate polymerization, while the position of a_2 peak is governed by the interatomic distance [63,71,75,76]. Therefore, the energy difference between the a_1 and a_2 peaks, $\Delta a_2 - a_1$, is related to the degree of polymerization (i.e., MCL) and to the Si—O bond length of C-(A-)S-H. The ascending trends of $\Delta a_2 - a_1$ and Si *K*-edge of C-A-S-H as the Ca/Si ratio decreases follows the same correlation of C-S-H, suggesting that the MCL increases with decreasing Ca/Si ratio. The value of $\Delta a_2 - a_1$ in C-A-S-H at each Ca/Si ratio is also slightly larger than the value of $\Delta a_2 - a_1$ in C-S-H (Fig. 5), which implies the increase in MCL by Al incorporation.

3.2.3. Ca/Si* = 1, Al/Si* = 0–0.1, and equilibrium at 7–80 °C

At each equilibration temperature, in addition to the increase in energy difference, $\Delta a_2 - a_1$, the Si *K*-edge of C-(A-)S-H shifts to higher energy with increasing Al/Si* ratio (Fig. 6 and Table 3). This suggests an elongation of aluminosilicates chains and marginal shortening of Si—O bonds, both resulting from Al uptake. The shoulder at ~1853.8–1855.8 eV (peak a_4) suggests that Q^3 and/or Q^3(1Al) sites occur in the C-A-S-H sample equilibrated at 80 °C [64]. The position of the Si *K*-edge of C-A-S-H is shifted to a markedly higher energy at 80 °C

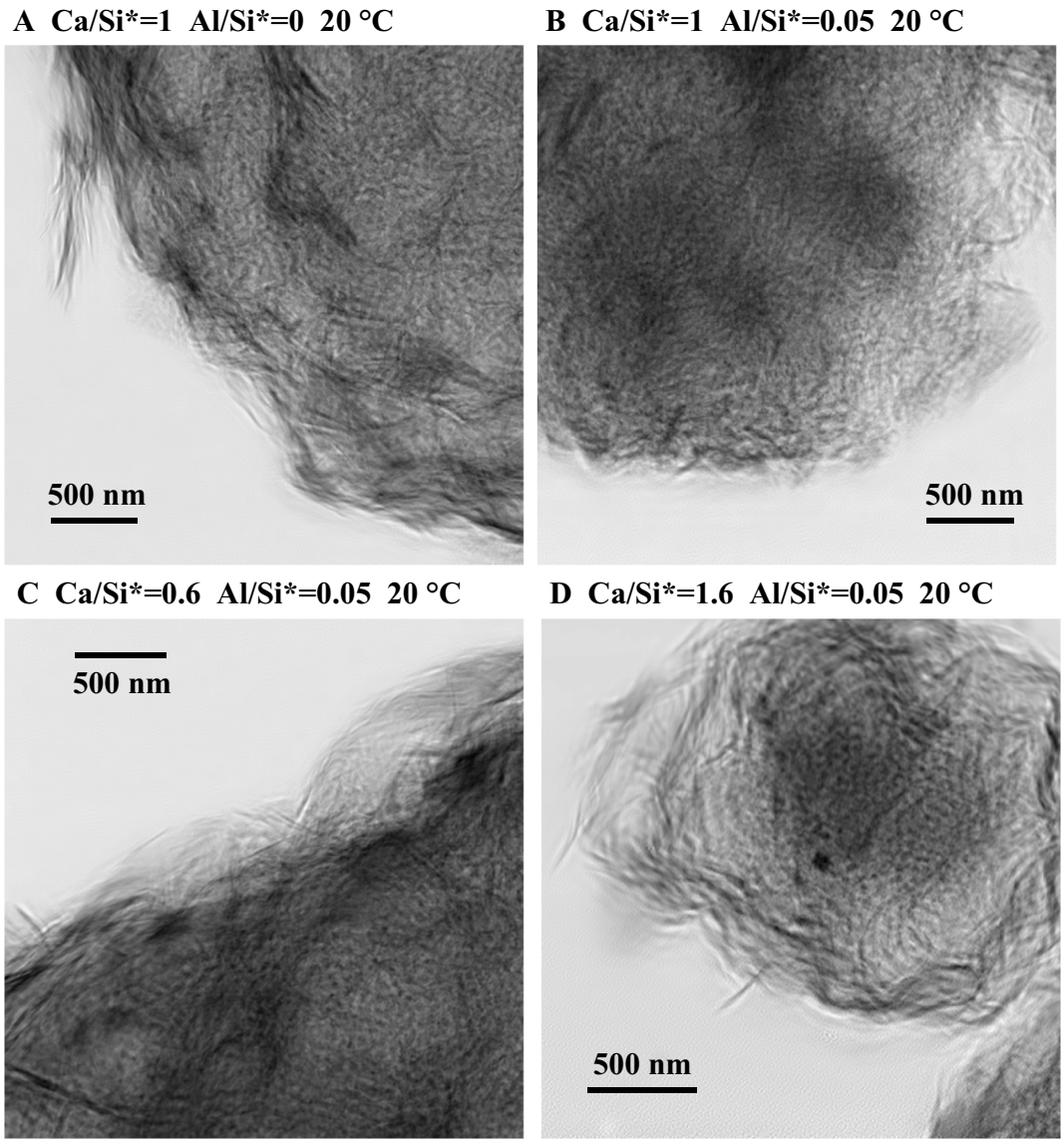

Fig. 8. Ptychographic magnitude images of C-(A-)S-H equilibrated at 20 °C for 182 days: A) Ca/Si* = 1.0, Al/Si* = 0; B) Ca/Si* = 1.0, Al/Si* = 0.05; C) Ca/Si* = 0.6, Al/Si* = 0.05; and D) Ca/Si = 1.6, Al/Si* = 0.05. Ca/Si* = bulk Ca/Si. Al/Si* = bulk Al/Si.

due to the occurrence of these Q^3 and Q^3(1Al) sites. The Si *K*-edge and $\Delta a_2 - a_1$ do not systematically vary across the equilibration temperature range of 7 to 80 °C, but do positively correlate with the MCL of C-(A-)S-H (Fig. 7). The trend is consistent with the relationship between the energies, Ca/Si ratio and MCL of C-(A-)S-H at 20 °C, i.e., the energies increase with increasing MCL and decreasing Si—O bond length. Two distinct Si *K*-edge spectra are differentiated in C-S-H products synthesized at 80 °C, which are assigned to tobermorite-like structures with average basal spacing of 13.8 Å and 12.1 Å (see Table A1, Supplementary information); the latter is more abundant in the sample, which is consistent with [77]. The relatively higher Si *K*-edge and $\Delta a_2 - a_1$ of C-S-H with 13.8 Å average basal spacing suggests that it has a longer MCL than the C-S-H phase with an average basal spacing of 12.1 Å.

3.3. Morphology of C-(A-)S-H

3.3.1. Effect of Ca/Si and Al inclusion at 20 °C

Ptychographic images of C-S-H (Ca/Si* = 1, equilibrated at 20 °C) show that this phase exhibits a crumpled foil-like morphology (Fig. 8A). The foils at the fringe of the grain represent high length-to-width aspect ratio. The interior of the particle is a network of multiple densely-packed foils. We expect that the features in this image represent the nature of C-S-H under ambient pressure. Richardson and Groves [35] observed similar morphological features in water-activated slag/PC paste by TEM. The C-S-H outer product formed in β-dicalcium silicate (β-Ca_2SiO_4, β-C_2S), tricalcium silicate (Ca_3SiO_5, C_3S), and PC pastes in studies using TEM [2,23,40] and ptychographic imaging [78] present fibers with more linear directional features. This is possibly due to much higher lime concentrations in the pore solutions of these materials and/or much greater space constraints (much lower water-to-solid ratio).

A recent TEM study showed that the C-S-H precipitated at Ca/Si* = 1 and using a similar water-to-solid ratio is also foil-like. The slight morphological difference of the C-S-H phase in that study relative to the present work can be attributed to different drying and vacuum conditions [79]. The morphology of C-S-H in hydrated C_3S in that study transitioned from foils to fibers as Ca concentration in solution increases [39].

A plateau (Fig. S2, Supplementary information) is observed in small angle scattering curve obtained from ptychographic image, suggesting the presence of concentrated packing of 'platelet' building blocks and

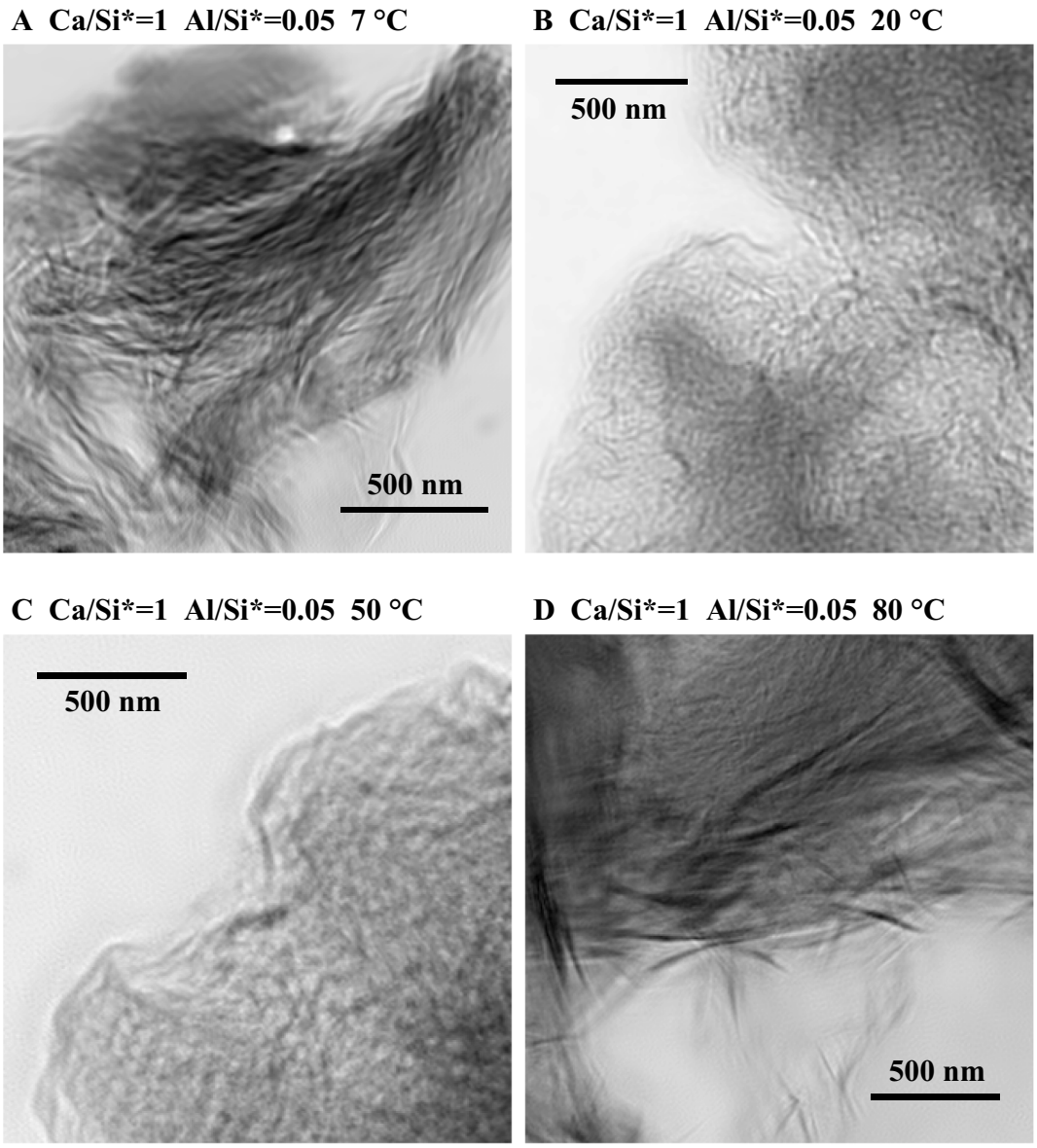

Fig. 9. Ptychographic magnitude images of C-A-S-H with Ca/Si* = 1 and Al/Si* = 0.05; A) equilibrated for 365 days at 7 °C; B) equilibrated for 182 days at 20 °C; C) equilibrated for 56 days at 50 °C; D) equilibrated for 56 days at 80 °C.

strong polydispersion [78]. We calculated the average thickness of this C-S-H platelet based on a lamellar model to be ~7 nm (from ptychographic magnitude image); therefore the average number of layers of the C-S-H platelets in the *c*-direction is ~5.6. A TEM study shows that C-S-H equilibrated at 20 °C from CaO-SiO_2-H_2O system is also foil-like at Ca/Si = 0.75–1.42, and the thickness of the foil is ~5–8 nm [39]. The distinction in thickness from the present work is expected due to different drying processes, vacuum conditions, and hydration ages.

Incorporation of Al into the C-A-S-H phase at 20 °C does not greatly alter its morphology, which is also identified as a network of crumpled foils. It appears similar to the outer product of water-activated slag hydrated for 3.5 years [2]. Variation in morphology of C-A-S-H (Al/Si* = 0.05, equilibrated at 20 °C) is not observed at Ca/Si* = 0.6, 1, 1.2, or 1.6 (Figs. 8 and S1 in Appendix B, Supplementary information), suggesting that the Ca/Si ratio does not significantly govern the nanomorphology of C-A-S-H equilibrated at 20 °C. We calculate the average thickness of C-A-S-H platelets at this temperature to be 5.9–7.3 nm (Appendix C, Supplementary information), which does not vary greatly as a function of the Ca/Si ratio, therefore the average number of layers of the C-A-S-H platelets ranges from ~4.3 to ~5.9. TEM micrographs by Rodriguez et al. [39] show that C-S-H synthesized in the CaO-SiO_2–H_2O system at 20 °C always appears to be foil-like regardless of Ca/Si. The slight morphological difference between the two studies can be attributed to the Al inclusion, drying process and other factors (e.g., vacuum condition and water-to-solid ratio).

3.3.2. *Effects of temperature and cross-linking*

The C-A-S-H phases (Ca/Si* = 1, Al/Si* = 0.05) precipitated using equilibration temperatures of 7 to 50 °C are morphologically similar (Fig. 9), while the morphologies of C-A-S-H phases appear to be significantly different at 80 °C (Fig. 10). The average thickness of C-A-S-H platelet is 5.3–6.5 nm for the 7–50 °C samples, while the average thickness of C-A-S-H for 80 °C samples is 14.5–14.7 nm (Appendix C, Supplementary information). Thus, the average number of stacked layers of the C-A-S-H platelets is ~4.8–5.3 for the 7–50 °C samples, while the average number of layers is 12.7–12.9 for the 80 °C samples. C-A-S-H samples with different Al/Si* ratios at 80 °C all present foil-predominant network, and the C-A-S-H at Al/Si* = 0.1 presents much thicker and wider agglomeration of foil structure than that at Al/Si* = 0.05. This observation shows that the Al incorporation at 80 °C

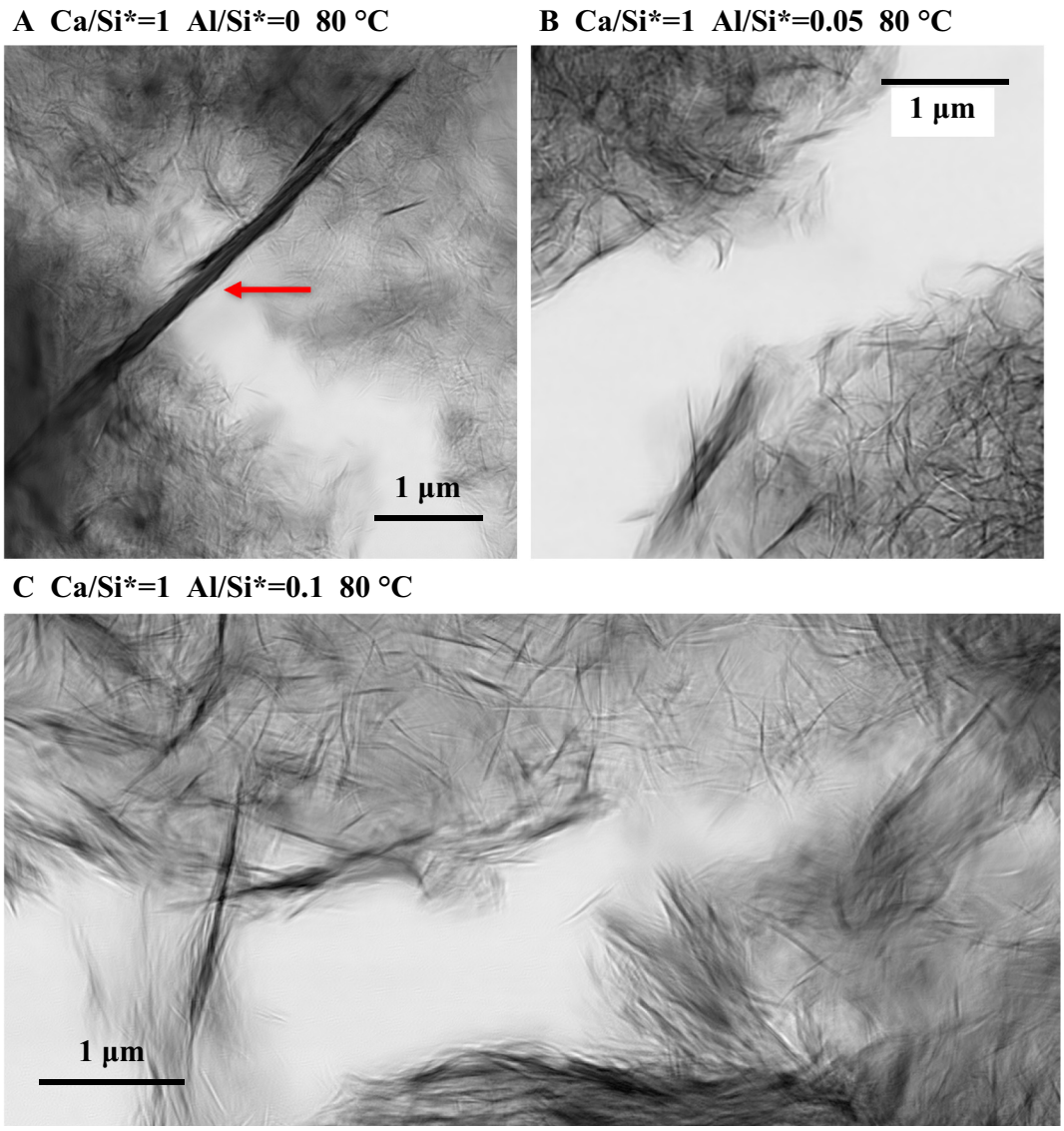

Fig. 10. A) Ptychographic magnitude images of C-(A-)S-H equilibrated for 56 days at 80 °C: A) Ca/Si* = 1, Al/Si* = 0; B) Ca/Si* = 1, Al/Si* = 0.05; C) Ca/Si* = 1, Al/Si* = 0.1. Tobermorite crystal with an average basal spacing of 13.8 Å is indicated by a red arrow. Ca/Si* = bulk Ca/Si. Al/Si* = bulk Al/Si. (For interpretation of the references to color in this figure legend, the reader is referred to the web version of this article.)

significantly alters the morphology of C-(A-)S-H. This effect is likely related to the increased crystalline order of this sample, although it may also be caused by its cross-linking of aluminosilicate chains and noticeably increased degree of C-A-S-H chain polymerization.

For samples equilibrated at 80 °C, the C-S-H foils are thinner and shorter than the C-A-S-H foils (both samples have Ca/Si* = 1.0). However, these foils are coarser than the C-(A-)S-H foils equilibrated at 7–50 °C (Ca/Si* = 1.0); the average basal spacing of the foils equilibrated at 80 °C is 12.1 Å (WAXS results in Appendix A, Supplementary information). SAS calculations confirm this significant change in morphology, which give an average stacked C-S-H platelet thickness for the 80 °C sample of 8.5 nm and an average number of layers of ~7. The coarse fibers with variable lengths ranging from hundreds of nanometers to a few microns in C-S-H at 80 °C correspond to a tobermorite-like structure with an average basal spacing of ~13.8 Å. The change in morphology in terms of elevated temperature is different from C-S-H gels in hydrated C_3S paste at 80 °C [23], which can be explained by the difference in the lime concentration of pore solution, space constraint and reaction kinetics.

3.4. A molecular-to-nanoscale model of C-A-S-H

A molecular-to-nanoscale model (Fig. 11) of the hypothetical C-A-S-H structure at equilibration temperature of 7 to 80 °C is proposed based on the results of coordination environment, morphology, and model fitting of SAS in terms of the stacked layer-structure. C-A-S-H equilibrated at 7–50 °C is structurally analogous to defective tobermorite, which contains CaO_7 sheets flanked with "dreierketten" – tetrahedral aluminosilicate chains – on one side and counter-ions (highly distorted six-fold coordinated Ca and five-fold coordinated Al) and water in an interlayer on the other. In this temperature range, cross-linked sites do not exist and Al is preferably incorporated at bridging sites (Q^2_B) of the aluminosilicate chains. The basal spacing of C-A-S-H structure varies from ~12 to 14 Å with varying Ca/Si ratios due to the Al-uptake and zeolitic content (Ca ions and water). The stacked thickness of lamellar building blocks of C-A-S-H at 7–50 °C ranges from 5.3 to 7.3 nm, representing ~4–6 stacked layers along the *c*-axis. Therefore, the building blocks constitute a network of crumpled densely-packed foils at the nanoscale.

Tetrahedral-coordinated Al also substitutes into cross-linked sites

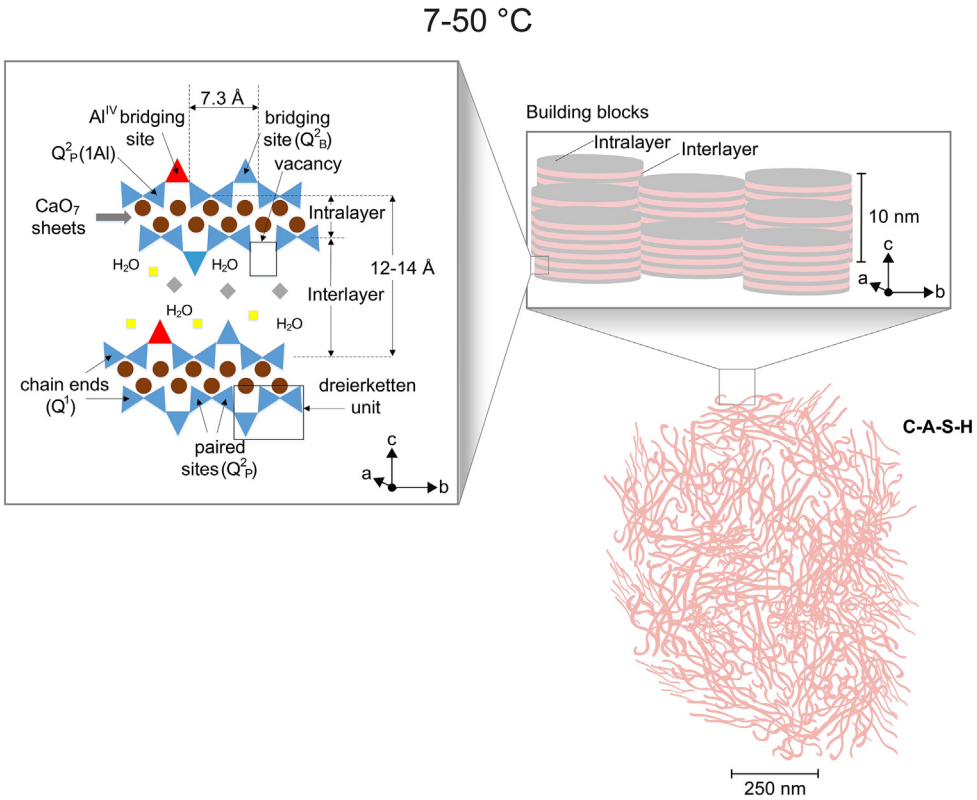

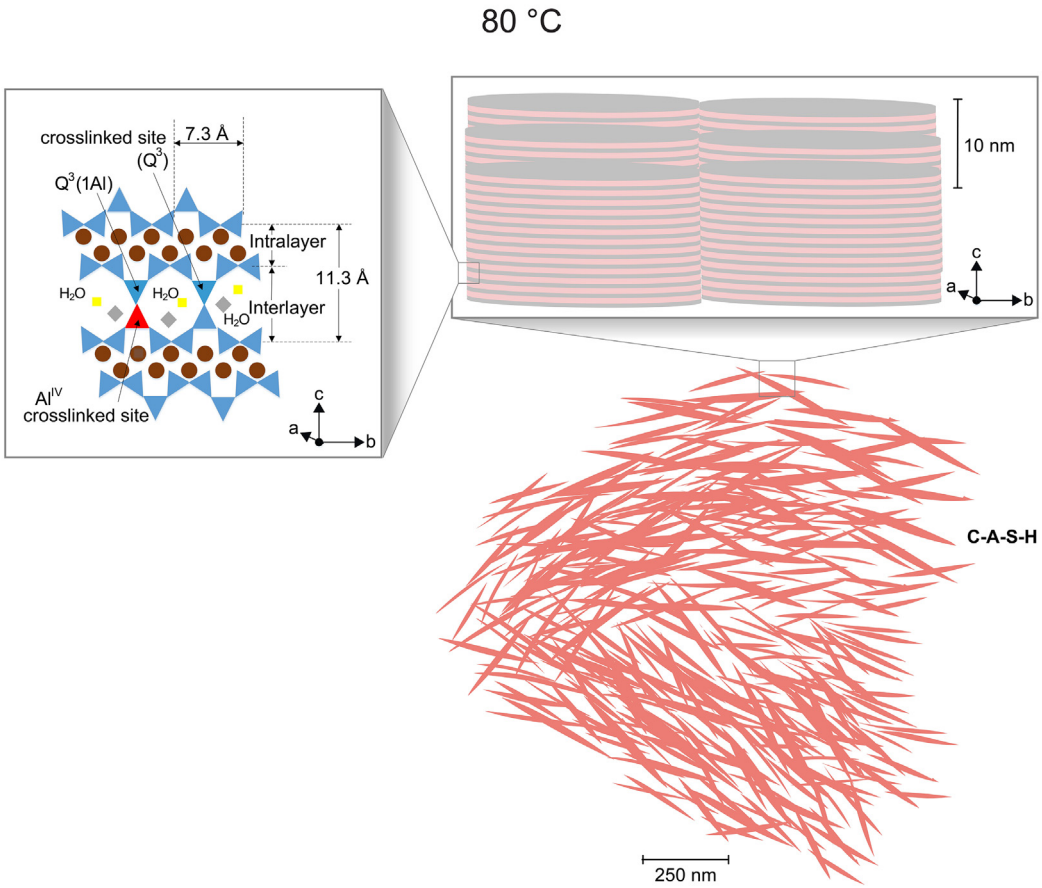

(caption on next page)

Fig. 11. Schematic diagram of nanocrystalline C-A-S-H (equilibration temperature of 7 to 80 °C). Brown circles represent Ca species in the CaO_7 sheets, and blue and red triangles denote SiO_4 and AlO_4 tetrahedron sites, respectively. The grey diamonds and yellow squares are counterions (e.g., Ca species and five-fold coordinated Al species) in the interlayer. Pink and grey alternating stacked layers of the building blocks represent interlayer and intralayer, respectively. Rouge foils denote the networking structure of C-A-S-H at the nanoscale. (For interpretation of the references to color in this figure legend, the reader is referred to the web version of this article.)

(Q^3) of chains in C-A-S-H equilibrated at 80 °C, which decreases the basal spacing to ~11.4 Å and significantly increases the polymerization of aluminosilicate chains. The elevated equilibration temperature does not alter the coordination symmetry of Ca species in C-A-S-H structure but triggers a longer-range of ordering of CaO_7 sheets. The average thickness of C-A-S-H building blocks at 80 °C is ~14.6 nm, denoting ~13 stacked layers along the *c*-axis. The coarser C-A-S-H building blocks constitute a foil-predominant network with less curvature and wider and thicker agglomeration at the nanoscale.

4. Conclusions

This paper has presented a synchrotron-based X-ray micro-spectroscopy study of C-(A-)S-H of different Ca/Si and Al/Si ratios, that were equilibrated at temperatures between 7 and 80 °C. The key conclusions are:

- Apart from the seven-fold coordinated Ca in the intralayer of C-(A-)S-H, the extra Ca that enters the interlayer are more likely six-fold coordinated in a distorted octahedral symmetry. The ordering of the Ca environment increases as Al content and equilibration temperature increase.
- Calcium environments in C-(A-)-S-H are similar to tobermorite. The coordination symmetry of Ca is highly distorted irrespective Ca/Si, Al uptake, and equilibration temperature.
- The Si *K*-edge shifts to higher energy with increased mean chain length of silicate chains. The energy separation between major and minor peak at the Si *K*-edge positively correlates with the degree of polymerization of its aluminosilicate chains.
- The Si—O bond length increases as the bulk Ca/Si ratio increases. Al incorporation leads to contraction of Si—O bonds in silicate tetrahedra in C-A-S-H.
- AFm-like species are not interstratified in the interlayer structure or precipitate on the external surface of C-A-S-H. TAH is either not Ca-bearing or its Ca is structurally similar to C-(A-)S-H. Al is preferably incorporated at bridging sites and is also accommodated in cross-linked bridging sites at 80 °C.
- C-S-H at Ca/Si* = 1 formed at 20 °C preferably presents crumpled foils with various lengths. The Al-uptake of C-S-H at 7–50 °C and Ca/Si ratio do not change its morphology. C-A-S-H equilibrated at 80 °C present coarser foils, and the foils are much thicker and longer with more Al inclusion.
- The building-block of all C-(A-)S-H samples is lamellar. C-A-S-H is morphologically similar with comparable lamellar thickness irrespective of Ca/Si or equilibration temperature at 7–50 °C. The lamellar thickness of C-S-H equilibrated at 80 °C is slightly enhanced, and the thickness is much greater with Al inclusion.

These results provide new insight into the morphology of C-(A-)S-H and the possible nature of TAH in C-A-S-H products, the coordination of Ca—O, and the environment of Si in C-(A-)S-H with different compositions and synthesized at different equilibration temperatures. Therefore, this paper yields an improved understanding of C-(A-)S-H chemistry, which will enhance the understanding of the performance of hydrated PC blends in service.

Acknowledgements

The authors thank Barbara Lothenbach for providing the C-(A-)S-H samples that were synthesized by Rupert J. Myers and Emilie L'Hôpital at the Laboratory for Concrete & Construction Chemistry (EMPA), Juan F.C. Vinasco for assistance with the STXM experiments, Sinem Ortaboy for helpful suggestions, and Tamika Bassman and Chen Li for the collaboration during the designing of Figures. This research is funded by the US National Science Foundation under the SusChEM Program, grant #DMR-1410557. This work is further supported by the Republic of Singapore National Research Foundation through a grant to the Berkeley Education Alliance for Research in Singapore (BEARS) for the Singapore-Berkeley Building Efficiency and Sustainability in the Tropics (SinBerBEST) Program. The Advanced Light Source is supported by the Director, Office of Science, Office of Basic Energy Sciences, of the U.S. Department of Energy under Contract No. DE-AC02-05CH11231.

Appendix A. Supplementary data

Supplementary data to this article can be found online at https://doi.org/10.1016/j.cemconres.2018.09.008.

References

[1] P.J. Monteiro, S.A. Miller, A. Horvath, Towards sustainable concrete, Nat. Mater. 16 (7) (2017) 698.
[2] I.G. Richardson, The nature of C-S-H in hardened cements, Cem. Concr. Res. 29 (8) (1999) 1131–1147.
[3] C. Li, H. Zhu, M. Wu, K. Wu, Z. Jiang, Pozzolanic reaction of fly ash modified by fluidized bed reactor-vapor deposition, Cem. Concr. Res. 92 (2017) 98–109.
[4] C. Li, M. Wu, Q. Chen, Z. Jiang, Chemical and mineralogical alterations of concrete subjected to chemical attacks in complex underground tunnel environments during 20–36 years, Cem. Concr. Compos. 86 (2018) 139–159.
[5] E. Bonaccorsi, S. Merlino, A.R. Kampf, The crystal structure of tobermorite 14 A (Plombierite), a C-S-H phase, J. Am. Ceram. Soc. 88 (3) (2005) 505–512.
[6] S. Merlino, E. Bonaccorsi, T. Armbruster, The real structure of tobermorite 11 angstrom: normal and anomalous forms, OD character and polytypic modifications, Eur. J. Mineral. 13 (3) (2001) 577–590.
[7] S. Merlino, E. Bonaccorsi, T. Armbruster, The real structures of clinotobermorite and tobermorite 9 angstrom: OD character, polytypes, and structural relationships, Eur. J. Mineral. 12 (2) (2000) 411–429.
[8] S. Merlino, E. Bonaccorsi, A.R. Kampf, Tobermorite 14 angstrom: crystal structure and OD character, Appl. Mineral. 1 and 2 (2000) 859–861.
[9] S. Merlino, E. Bonaccorsi, T. Armbruster, Tobermorites: their real structure and order-disorder (OD) character, Am. Mineral. 84 (10) (1999) 1613–1621.
[10] S. Ortaboy, J. Li, G. Geng, R.J. Myers, P.J. Monteiro, R. Maboudian, C. Carraro, Effects of CO 2 and temperature on the structure and chemistry of C–(A–) S–H investigated by Raman spectroscopy, RSC Adv. 7 (77) (2017) 48925–48933.
[11] G. Renaudin, J. Russias, F. Leroux, C. Cau-dit-Coumes, F. Frizon, Structural characterization of C–S–H and C–A–S–H samples—part II: local environment investigated by spectroscopic analyses, J. Solid State Chem. 182 (12) (2009) 3320–3329.
[12] X. Pardal, F. Brunet, T. Charpentier, I. Pochard, A. Nonat, 27Al and 29Si solid-state NMR characterization of calcium-aluminosilicate-hydrate, Inorg. Chem. 51 (3) (2012) 1827–1836.
[13] G. Sun, J.F. Young, R.J. Kirkpatrick, The role of Al in C–S–H: NMR, XRD, and compositional results for precipitated samples, Cem. Concr. Res. 36 (1) (2006) 18–29.
[14] E. L'Hôpital, B. Lothenbach, G. Le Saout, D. Kulik, K. Scrivener, Incorporation of aluminium in calcium-silicate-hydrates, Cem. Concr. Res. 75 (2015) 91–103.
[15] P. Faucon, A. Delagrave, J. Petit, C. Richet, J. Marchand, H. Zanni, Aluminum incorporation in calcium silicate hydrates (CSH) depending on their Ca/Si ratio, J. Phys. Chem. B 103 (37) (1999) 7796–7802.
[16] X. Pardal, I. Pochard, A. Nonat, Experimental study of Si–Al substitution in calcium-silicate-hydrate (CSH) prepared under equilibrium conditions, Cem. Concr. Res. 39 (8) (2009) 637–643.
[17] A. Brough, A. Atkinson, Sodium silicate-based, alkali-activated slag mortars: part I. Strength, hydration and microstructure, Cem. Concr. Res. 32 (6) (2002) 865–879.
[18] R.J. Myers, S.A. Bernal, R. San Nicolas, J.L. Provis, Generalized structural description of calcium–sodium aluminosilicate hydrate gels: the cross-linked substituted tobermorite model, Langmuir 29 (17) (2013) 5294–5306.
[19] R.J. Myers, S.A. Bernal, J.D. Gehman, J.S. Deventer, J.L. Provis, The role of Al in cross-linking of alkali-activated slag cements, J. Am. Ceram. Soc. 98 (3) (2015)

996–1004.
[20] A. Vollpracht, B. Lothenbach, R. Snellings, J. Haufe, The pore solution of blended cements: a review, Mater. Struct. 49 (8) (2016) 3341–3367.
[21] S. Hamid, The crystal structure of the 11 Ä natural tobermorite Ca2.25[Si3O7.5(OH)1.5]·1H2O, Z. Krist. Cryst. Mater. 154 (1–4) (1981) 189–198.
[22] M.W. Grutzeck, A new model for the formation of calcium silicate hydrate (C–S–H), Mater. Res. Innov. 3 (3) (1999) 160–170.
[23] I.G. Richardson, Tobermorite/jennite- and tobermorite/calcium hydroxide-based models for the structure of C–S–H: applicability to hardened pastes of tricalcium silicate, beta-dicalcium silicate, Portland cement, and blends of Portland cement with blast-fumace slag, metakaolin, or silica fume, Cem. Concr. Res. 34 (9) (2004) 1733–1777.
[24] Y. Zhou, D. Hou, J. Jiang, W. She, J. Li, Molecular dynamics study on the solvated aniline (AN) and ethylene glycol (EG) monomers confined in calcium silicate nanometer channel: a case study of Tobermorite, Phys. Chem. Chem. Phys. 19 (2017) 15145–15159.
[25] R.J.-M. Pellenq, A. Kushima, R. Shahsavari, K.J. Van Vliet, M.J. Buehler, S. Yip, F.-J. Ulm, A realistic molecular model of cement hydrates, Proc. Natl. Acad. Sci. 106 (38) (2009) 16102–16107.
[26] N. Lequeux, A. Morau, S. Philippot, P. Boch, Extended X-ray absorption fine structure investigation of calcium silicate hydrates, J. Am. Ceram. Soc. 82 (5) (1999) 1299–1306.
[27] C. Biagioni, S. Merlino, E. Bonaccorsi, The tobermorite supergroup: a new nomenclature, Mineral. Mag. 79 (2) (2015) 485–495.
[28] C. Biagioni, E. Bonaccorsi, S. Merlino, D. Bersani, New data on the thermal behavior of 14 angstrom tobermorite, Cem. Concr. Res. 49 (2013) 48–54.
[29] S. Merlino, E. Bonaccorsi, M. Merlini, F. Marchetti, W. Garra, Tobermorite 11 angstrom and its synthetic counterparts: structural relationships and thermal behaviour, Miner. Adv. Materi. I (2008) 37–44.
[30] E. Bonaccorsi, S. Merlino, Crystal chemistry and structural arrangements of 'normal' and 'anomalous' tobermorite 11 angstrom, Appl. Mineral. 1 and 2 (2000) 735–738.
[31] R.J. Kirkpatrick, G.E. Brown, N. Xu, X.D. Cong, Ca X-ray absorption spectroscopy of C–S–H and some model compounds, Adv. Cem. Res. 9 (33) (1997) 31–36.
[32] S. Soyer-Uzun, S.R. Chae, C.J. Benmore, H.R. Wenk, P.J.M. Monteiro, Compositional evolution of calcium silicate hydrate (C–S–H) structures by total X-ray scattering, J. Am. Ceram. Soc. 95 (2) (2012) 793–798.
[33] I.L. Moudrakovski, R. Alizadeh, J.J. Beaudoin, Natural abundance high field 43Ca solid state NMR in cement science, Phys. Chem. Chem. Phys. 12 (26) (2010) 6961–6969.
[34] I.G. Richardson, Model structures for C–(A)–SH (I), Acta Crystallogr. Sect. B: Struct. Sci. Cryst. Eng. Mater. 70 (6) (2014) 903–923.
[35] I.G. Richardson, G.W. Groves, Microstructure and microanalysis of hardened cement pastes involving ground granulated blast-furnace slag, J. Mater. Sci. 27 (22) (1992) 6204–6212.
[36] R. Taylor, I.G. Richardson, R.M.D. Brydson, Composition and microstructure of 20-year-old ordinary Portland cement-ground granulated blast-furnace slag blends containing 0 to 100% slag, Cem. Concr. Res. 40 (7) (2010) 971–983.
[37] I.G. Richardson, The calcium silicate hydrates, Cem. Concr. Res. 38 (2) (2008) 137–158.
[38] I.G. Richardson, The nature of the hydration products in hardened cement pastes, Cem. Concr. Compos. 22 (2) (2000) 97–113.
[39] E.T. Rodriguez, I.G. Richardson, L. Black, E. Boehm-Courjault, A. Nonat, J. Skibsted, Composition, silicate anion structure and morphology of calcium silicate hydrates (C–S–H) synthesised by silica-lime reaction and by controlled hydration of tricalcium silicate (C3S), Adv. Appl. Ceram. 114 (7) (2015) 362–371.
[40] I.G. Richardson, G.W. Groves, Microstructure and microanalysis of hardened ordinary Portland-cement pastes, J. Mater. Sci. 28 (1) (1993) 265–277.
[41] G. Geng, J. Li, Y.-S. Yu, D.A. Shapiro, D.A. Kilcoyne, P.J. Monteiro, Nanometer-resolved spectroscopic study reveals the conversion mechanism of CaO·Al2O3·10H2O to 2CaO·Al2O3·8H2O and 3CaO·Al2O3·6H2O at an elevated temperature, Cryst. Growth Des. 17 (8) (2017) 4246–4253.
[42] J.C. da Silva, P. Trtik, A. Diaz, M. Holler, M. Guizar-Sicairos, J.r. Raabe, O. Bunk, A. Menzel, Mass density and water content of saturated never-dried calcium silicate hydrates, Langmuir 31 (13) (2015) 3779–3783.
[43] G.Q. Geng, R. Taylor, S. Bae, D. Hernandez-Cruz, D.A. Kilcoyne, A.H. Emwas, P.J.M. Monteiro, Atomic and nano-scale characterization of a 50-year-old hydrated C3S paste, Cem. Concr. Res. 77 (2015) 36–46.
[44] Q. Li, Y. Ge, G. Geng, S. Bae, P.J.M. Monteiro, CaCl2-accelerated hydration of tricalcium silicate: a STXM study combined with 29Si MAS NMR, J. Nanomater. 2015 (2015) 1–10.
[45] S. Bae, R. Taylor, D. Hernandez-Cruz, S. Yoon, D. Kilcoyne, P.J.M. Monteiro, Soft X-ray spectromicroscopic investigation of synthetic C–S–H and C3S hydration products, J. Am. Ceram. Soc. 98 (9) (2015) 2914–2920.
[46] R.J. Myers, E. L'Hopital, J.L. Provis, B. Lothenbach, Effect of temperature and aluminium on calcium (alumino)silicate hydrate chemistry under equilibrium conditions, Cem. Concr. Res. 68 (2015) 83–93.
[47] A.L.D. Kilcoyne, T. Tyliszczak, W.F. Steele, S. Fakra, P. Hitchcock, K. Franck, E. Anderson, B. Harteneck, E.G. Rightor, G.E. Mitchell, A.P. Hitchcock, L. Yang, T. Warwick, H. Ade, Interferometer-controlled scanning transmission X-ray microscopes at the Advanced Light Source, J. Synchrotron Radiat. 10 (2003) 125–136.
[48] D. Kilcoyne, et al., A new scanning transmission X-ray microscope at the ALS for operation up to 2500 eV, AIP Conference Proceedings, 2010, p. 465.
[49] S.J. Naftel, T.K. Sham, Y.M. Yiu, B.W. Yates, Calcium L-edge XANES study of some calcium compounds, J. Synchrotron Radiat. 8 (2001) 255–257.
[50] J.P. Ko, X-ray absorption near-edge structure (XANES) of calcium L3,2 edges of various calcium compounds and X-ray excited optical luminescence (XEOL) studies of luminescent calcium compounds, X-ray Absorption Fine Structure—XAFS, vol. 13(882), 2007, pp. 538–540.
[51] F.M.F. Degroot, J.C. Fuggle, B.T. Thole, G.A. Sawatzky, 2p X-ray absorption of 3d transition-metal compounds - an atomic multiplet description including the crystal-field, Phys. Rev. B 42 (9) (1990) 5459–5468.
[52] G. Geng, R.J. Myers, A.L. Kilcoyne, J. Ha, P.J. Monteiro, Ca L2, 3-edge near edge X-ray absorption fine structure of tricalcium aluminate, gypsum, and calcium (sulfo) aluminate hydrates, Am. Mineral. 102 (4) (2017) 900–908.
[53] M.E. Fleet, X.Y. Liu, Calcium L-2,L-3-edge XANES of carbonates, carbonate apatite, and oldhamite (CaS), Am. Mineral. 94 (8–9) (2009) 1235–1241.
[54] S. Hanhan, A.M. Smith, M. Obst, A.P. Hitchcock, Optimization of analysis of soft X-ray spectromicroscopy at the Ca 2p edge, J. Electron Spectrosc. Relat. Phenom. 173 (1) (2009) 44–49.
[55] E. L'Hôpital, B. Lothenbach, K. Scrivener, D. Kulik, Alkali uptake in calcium alumina silicate hydrate (CASH), Cem. Concr. Res. 85 (2016) 122–136.
[56] E. L'Hôpital, B. Lothenbach, D. Kulik, K. Scrivener, Influence of calcium to silica ratio on aluminium uptake in calcium silicate hydrate, Cem. Concr. Res. 85 (2016) 111–121.
[57] C.S. Walker, D. Savage, M. Tyrer, K.V. Ragnarsdottir, Non-ideal solid solution aqueous solution modeling of synthetic calcium silicate hydrate, Cem. Concr. Res. 37 (4) (2007) 502–511.
[58] G.Q. Geng, R.J. Myers, M.J.A. Qomi, P.J.M. Monteiro, Densification of the interlayer spacing governs the nanomechanical properties of calcium-silicate-hydrate, Sci. Rep. 7 (2017).
[59] E. Gartner, I. Maruyama, J. Chen, A new model for the CSH phase formed during the hydration of Portland cements, Cem. Concr. Res. 97 (2017) 95–106.
[60] L. Black, K. Garbev, G. Beuchle, P. Stemmermann, D. Schild, X-ray photoelectron spectroscopic investigation of nanocrystalline calcium silicate hydrates synthesised by reactive milling, Cem. Concr. Res. 36 (6) (2006) 1023–1031.
[61] G. Renaudin, J. Russias, F. Leroux, F. Frizon, C. Cau-dit-Coumes, Structural characterization of C–S–H and C–A–S–H samples—part I: long-range order investigated by Rietveld analyses, J. Solid State Chem. 182 (12) (2009) 3312–3319.
[62] M.D. Andersen, H.J. Jakobsen, J. Skibsted, A new aluminium-hydrate species in hydrated Portland cements characterized by 27 Al and 29 Si MAS NMR spectroscopy, Cem. Concr. Res. 36 (1) (2006) 3–17.
[63] D. Li, G.M. Bancroft, M.E. Fleet, X.H. Feng, Silicon K-edge XANES spectra of silicate minerals, Phys. Chem. Miner. 22 (2) (1995) 115–122.
[64] D. Cabaret, M. Le Grand, A. Ramos, A.M. Flank, S. Rossano, L. Galoisy, G. Calas, D. Ghaleb, Medium range structure of borosilicate glasses from Si K-edge XANES: a combined approach based on multiple scattering and molecular dynamics calculations, J. Non-Cryst. Solids 289 (1–3) (2001) 1–8.
[65] D. Li, Aluminum, Silicon, Phosphorus and Sulfur K- and L-edge X-ray Absorption Spectroscopy of Minerals and Glasses: Applications in Mineralogy and Geochemistry, (1994), p. 2432 (PhD thesis).
[66] G.S. Henderson, M.E. Fleet, The structure of titanium silicate glasses investigated by Si K-edge X-ray absorption spectroscopy, J. Non-Cryst. Solids 211 (3) (1997) 214–221.
[67] A. Bianconi, M. Dellariccia, P.J. Durham, J.B. Pendry, Multiple-scattering resonances and structural effects in the X-ray-absorption near-edge spectra of Fe-II and Fe-III hexacyanide complexes, Phys. Rev. B 26 (12) (1982) 6502–6508.
[68] G. Bunker, Introduction to XAFS: A Practical Guide to X-ray Absorption Fine Structure Spectroscopy, Cambridge University Press, 2010.
[69] K.A. Smith, R.J. Kirkpatrick, E. Oldfield, D.M. Henderson, High-resolution silicon-29 nuclear magnetic resonance spectroscopic study of rock-forming silicates, Am. Mineral. 68 (11–12) (1983) 1206–1215.
[70] R. Hill, G. Gibbs, Variation in d (TO), d (T···T) and ∠TOT in silica and silicate minerals, phosphates and aluminates, Acta Crystallogr. B Struct. Crystallogr. Cryst. Chem. 35 (1) (1979) 25–30.
[71] G.S. Henderson, A Si K-edge EXAFS/XANES study of sodium-silicate glasses, J. Non-Cryst. Solids 183 (1–2) (1995) 43–50.
[72] P. Yu, R.J. Kirkpatrick, B. Poe, P.F. McMillan, X.D. Cong, Structure of calcium silicate hydrate (C–S–H): near-, mid-, and far-infrared spectroscopy, J. Am. Ceram. Soc. 82 (3) (1999) 742–748.
[73] K. Garbev, P. Stemmermann, L. Black, C. Breen, J. Yarwood, B. Gasharova, Structural features of C–S–H(I) and its carbonation in air - a Raman spectroscopic study. Part I: fresh phases, J. Am. Ceram. Soc. 90 (3) (2007) 900–907.
[74] L. Black, K. Garbev, P. Stemmermann, K.R. Hallam, G.C. Allen, Characterisation of crystalline C-S-H phases by X-ray photoelectron spectroscopy, Cem. Concr. Res. 33 (6) (2003) 899–911.
[75] D. Li, G.M. Bancroft, M. Kasrai, M.E. Fleet, X.H. Feng, K.H. Tan, B.X. Yang, High-resolution Si K-edge and L2,3-edge XANES of alpha-quartz and stishovite, Solid State Commun. 87 (7) (1993) 613–617.
[76] D. Li, G.M. Bancroft, M. Kasrai, M.E. Fleet, R.A. Secco, X.H. Feng, K.H. Tan, B.X. Yang, X-ray-absorption spectroscopy of silicon dioxide (SiO2) polymorphs - the structural characterization of opal, Am. Mineral. 79 (7–8) (1994) 622–632.
[77] G. Geng, R.J. Myers, J. Li, R. Maboudian, C. Carraro, D.A. Shapiro, P.J. Monteiro, Aluminum-induced dreierketten chain cross-links increase the mechanical properties of nanocrystalline calcium aluminosilicate hydrate, Sci. Rep. 7 (2017) 44032.
[78] S. Bae, R. Taylor, D. Shapiro, P. Denes, J. Joseph, R. Celestre, S. Marchesini, H. Padmore, T. Tyliszczak, T. Warwick, Soft X-ray ptychographic imaging and morphological quantification of calcium silicate hydrates (C–S–H), J. Am. Ceram. Soc. 98 (12) (2015) 4090–4095.
[79] P. Fonseca, H.M. Jennings, The effect of drying on early-age morphology of C–S–H as observed in environmental SEM, Cem. Concr. Res. 40 (12) (2010) 1673–1680.